

A Single-shot Camera-Projector Calibration System For Imperfect Planar Targets

Bingyao Huang^{*}
Temple Univeristy

Samed Ozdemir[†]
Rowan Univeristy

Ying Tang[‡]
Rowan Univeristy

Haibin Ling[§]
Temple Univeristy

ABSTRACT

Existing camera-projector calibration methods typically warp feature points from a camera image to a projector image using estimated homographies, and often suffer from errors in camera parameters and noise due to imperfect planarity of the calibration target. In this paper we propose a simple yet robust solution that explicitly deals with these challenges. Following the structured light (SL) camera-project calibration framework, a carefully designed correspondence algorithm is built on top of the De Bruijn patterns. Such correspondence is then used for initial camera-projector calibration. Then, to gain more robustness against noises, especially those from an imperfect planar calibration board, a novel bundle adjustment algorithm is developed to jointly optimize the estimated camera and projector models. Aside from the robustness, our solution requires only one shot of SL pattern for each calibration board pose, which is much more convenient than multi-shot solutions in practice. Data validations are conducted on both synthetic and real datasets, and our method shows clear advantages over existing methods in all experiments.

Index Terms: Computing methodologies—Camera calibration; Computing methodologies—3D imaging; Computing methodologies—Reconstruction

1 INTRODUCTION

Camera-projector systems are popular in 3D surface reconstruction and naked eye augmented reality, where in most cases, structured light (SL) is applied due to its ease of use and accuracy. Compared with passive feature point based 3D reconstruction methods, such as stereo vision and structure from motion (SfM), SL is able to reconstruct a denser and more precise surface. Moreover, SL works for texture-less or repetitively textured objects.

A typical SL system consists of a calibrated camera and projector pair placed at a fixed distance and orientation as shown in Fig. 1. Firstly, the projector projects known encoded patterns onto the target object, then the projected patterns are deformed according to the surface shape of the target object. Once the camera captures the deformed patterns, pixel correspondences between camera and projector can be established by matching the captured and projected patterns. In the end, the 3D coordinates of the deformed pattern pixels are triangulated, given the camera-projector parameters and pixel correspondences.

Despite the simplicity, the 3D reconstruction precision of an SL system is highly dependent on the joint camera-projector pair calibration. Unlike a binocular stereo vision system, in an SL system, the projector is unable to capture images. So most SL calibration systems model the projector as a reverse camera that can “see” the

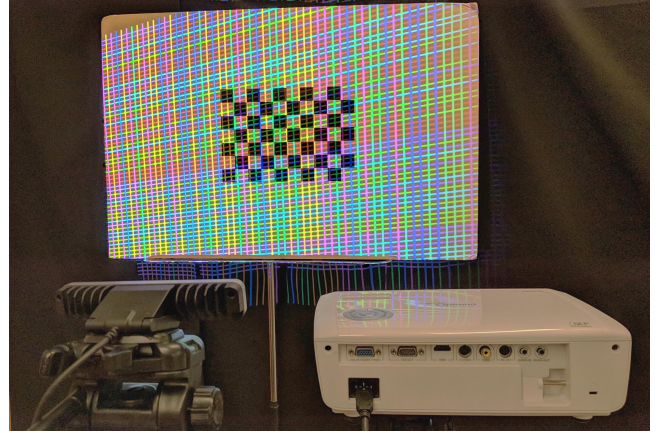


Figure 1: System setup: a projector on the bottom-right, a camera on the bottom-left and calibration board with a checkerboard pattern attached to it.

calibration target [4, 17, 32]. Then it can be simply calibrated like a camera using Zhang’s method [34].

The above camera-projector framework requires correspondences between the projector image plane and a reference plane, which is usually approximated by a planar calibration board with a printed checkerboard, dots or circles pattern. The camera can be calibrated using these patterns. Afterwards, the projector projects encoded SL patterns onto the calibration board, and these SL patterns are then captured by the camera for calibrating the projector.

In practice, the calibration board and printed pattern are hardly perfect planar due to manufacturing and/or glue. As pointed out by [1, 12, 24, 25, 34], an imperfect calibration target may significantly impact the accuracy of Zhang’s method. As most existing calibration methods rely on camera parameters to warp printed feature points to the projector image space, the camera error may be propagated to the projector image plane. This adds to the error of projector calibration that is again done by Zhang’s method.

To address this issue, we propose a novel additional step to jointly rectify the camera and projector models. Specifically, after calibrating the camera and projector using the traditional method, we put them into a bundle adjustment (BA) framework for rectification, together with a scale regularization for further improvement. Another key component in our system is the reliable correspondence construction process. By using an efficient De Bruijn pattern and a carefully designed keypoint extraction algorithm, our system provides reliable keypoint correspondence for the calibration algorithms. Moreover, being a single-shot solution, our system brings practical convenience over systems that require multiple shots of SL patterns for a single calibration board pose. This is particularly important for applications that require frequent re-calibrations, e.g., with the camera/projector moving around.

To summarize, our system brings the following contributions and benefits:

^{*}e-mail: bingyao.huang@temple.edu

[†]e-mail: ozdemi63@students.rowan.edu

[‡]e-mail: tang@rowan.edu

[§]e-mail: hbling@temple.edu

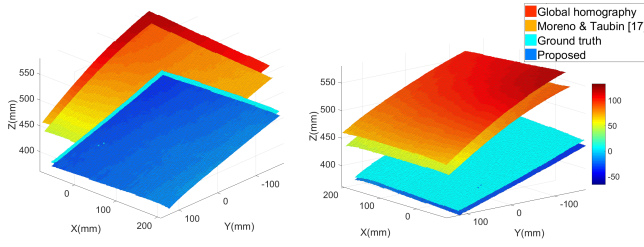


Figure 2: Reconstructed planes: bottom view (left) and top view (right), including a global homography calibration method (red), the Moreno & Taubin’s method [17] (Orange), the proposed method (blue), and the ground truth (cyan). Reconstruction errors in the Z direction are coded in color.

- Our system explicitly deals with the noise in target planarity with a novel BA solution. This is the first such system for joint camera-projector calibration, to the best of our knowledge.
- Unlike many existing methods, to calibrate the system, we apply points from an SL pattern rather than from a checkerboard. This strategy boosts not only the number of feature points but also their spatial distribution, and hence improves calibration robustness.
- The proposed method performs camera-projector pair calibration with only a single-shot, making it practically convenient in many applications. It can provide a flexible and accurate results even when the board is handheld.

The effectiveness of the proposed solution over existing ones is clearly demonstrated in our experiments on both synthetic and real data, especially when the calibration board is imperfect planar (Fig. 2). In addition, the source code is publicly available at <https://github.com/BingyaoHuang/single-shot-pro-cam-calib>.

In the rest of the paper, we summarize related work in Sect. 2 and introduce our camera-projector calibration method in Sect. 3. Then, we report the experimental validation in Sect. 4, and finally conclude this paper in Sect. 5.

2 RELATED WORK

Most existing camera-projector pair calibration methods apply Zhang’s method [34], where the 3D-2D correspondences between the points on the calibration board and the projector image are computed by some transformations. Regardless of a multi-shot or single-shot method, their transformations fall into one of the following methods: global homography [2, 7–9, 13, 14, 18, 19, 30], local homography [16, 17], direct pixel-to-pixel transformation [32] and incremental projector image pre-warp [3, 6, 23, 29, 33].

It is worth noting that a global homography based method usually ignores both projector lens distortions and imperfect planarity of the calibration board. While the other three types of calibration methods can model projector lens distortion [6, 16, 17, 32, 33], they are highly dependent on camera calibration accuracy. In addition, the imperfect planarity of calibration board is ignored in all the reviewed methods above, and such imperfectness can cause errors as pointed out in [1, 12, 24, 25, 34] and illustrated in Fig. 2.

Other than using Zhang’s method, self-calibration algorithms [15, 27, 28, 30] are capable of calibrating intrinsics and extrinsics of the camera-projector pair without a known planar target, instead a fundamental matrix or its variant is estimated using camera and projector image correspondences. With some priori of the intrinsics, e.g., unit aspect ratio and the principle point is assumed to be at

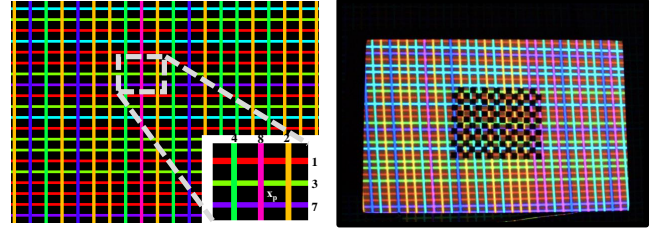


Figure 3: Projected (left) and camera captured (right) color-coded SL pattern. Best viewed in color.

the center of the image. However, these two assumptions are often violated, especially for projectors [17].

Additional cameras can also be included to either reduce calibration board poses [5] or allow arbitrary shapes as calibration targets [21]. However, these methods are even inflexible since they either require additional hardware or precise 3D measurement of a complex object, let alone multiple shots.

Multi-shot and single-shot methods According to [10], we categorize SL-based camera-projector calibration methods into two types: multi-shot [5, 6, 17, 20, 27–29, 32] and single-shot [2, 4, 30, 31]. Specifically, multi-shot and single-shot indicate the number of SL pattern shots required for *each* calibration board pose, rather than the total number of shots of the whole calibration process.

Multi-shot methods project a sequence of patterns onto the calibration board, the patterns are encoded in Gray/binary code [17, 20, 27] or multiple phase shifting [32], leading to a pixel-wise or even sub-pixel resolution. However, a disadvantage is that it is slow and computationally expensive due to multiple shots, e.g., [17] requires about 20 shots and captures for each pose. Incremental methods [3, 6, 16, 23, 29, 33] also belong to multi-shot, since the projected pattern is incrementally adjusted to fit the printed pattern until a perfect superimposition is achieved, which requires at least two shots per pose.

Despite the correspondence accuracy, multi-shot calibration methods are both computationally expensive and memory inefficient compared with single-shot ones. Moreover, multi-shot methods are sensitive to motion; even a little shift or jitter between two consecutive captures can produce huge SL decoding errors due to pattern misalignment. For example, when a user holds the calibration board or a mobile camera-projector pair, it is very hard to ensure absolute stillness of the target between consecutive shots.

Single-shot methods adopt spatial multiplexed patterns including the De Bruijn sequence [11, 22, 31], M-array [4, 30], checkerboard [2] and phase shifting fringes. The feature point correspondences are uniquely encoded in a single SL pattern. Consequently, single-shot SL allows for faster and more flexible camera-projector calibration than multi-shot SL.

Compared with previous studies, our camera-projector calibration is simple and fast, and requires only one shot per calibration board pose. Moreover, it refines imperfectly calibrated camera and projector parameters due to imperfect planar calibration board using a bundle adjustment method. The experiments show that our method outperforms the other counterparts on both synthetic and real data.

3 METHOD

Notations. Throughout the paper, we use the mathematical notations as shown in Table 1. In addition we use subscripts c , p and m for camera, projector and calibration board model space, respectively. Thus, the subscript cp (or mp) stands for the transformation from camera (or calibration board) coordinate system to projector coordinate system (Fig. 4).

Table 1: Notations

Notation	Example	Meaning
italic	a, A, \dots	scalars
lower-case boldface	$\mathbf{a}, \mathbf{b}, \dots$	vectors
boldface capital	$\mathbf{A}, \mathbf{B}, \dots$	matrices
calligraphic	$\mathcal{A}, \mathcal{B}, \dots$	sets
index range	$\mathbf{a}^{1:N}$	$\mathbf{a}^1, \mathbf{a}^2, \dots, \mathbf{a}^N$
dot	$\dot{\mathbf{a}}, \dot{\mathbf{A}}, \dots$	initial guess
hat	$\hat{\mathbf{a}}, \hat{\mathbf{A}}, \dots$	estimation
bar	$\bar{\mathbf{a}}, \bar{\mathbf{A}}, \dots$	homogeneous coordinates

3.1 System Overview

Our camera-projector calibration system (Fig. 1) consists of an RGB camera, a projector and a white board with a printed checkerboard pattern attached to it. As summarized in Algorithm 1, it contains three stages: (1) initial camera calibration using checkerboard images, (2) initial projector calibration using projected SL patterns, and (3) joint refinement of camera and projector parameters using bundle adjustment (BA).

As shown in the system flowchart in Fig. 5, we start by capturing an image of the calibration board, then we project a color-encoded SL pattern to the calibration board and take an image of the superimposed SL pattern. We change the pose of the calibration board manually and repeat the steps above to get sufficient pose samples. Then, we first calibrate the camera using Zhang’s method to get the initial camera model, including camera intrinsics and rotations and translations of each calibration board pose relative to the camera.

We then undistort the captured SL images. After that, we decode the SL patterns in the camera image plane and find their correspondences to the original SL pattern in the projector image plane (Sect. 3.3). Following that, we transform the SL points to the calibration board model space using rotations and translations obtained in last step. Note the SL points in the calibration board model space may also be erroneous due to inaccurate camera calibration. With these correspondences, we apply Zhang’s method again to calibrate the projector. The relative rotation and translation between camera and projector are estimated using stereo calibration (Equation 3.4). Similar to camera parameters, the projector parameters obtained are also initial guesses and subject to propagated errors from camera calibration and imperfect planarity of the calibration board.

Finally, we gather camera and projector parameters along with the SL points to perform a BA refinement. This last step largely reduces errors in initial calibration (Sect. 3.5).

3.2 Structured Light Pattern

To allow for the single-shot calibration, we employ a spatial multiplexed SL technique, and use only a single color-encoded pattern (Fig. 3). The SL pattern is a variant of [22] and is composed of vertical and horizontal colored stripes with a De Bruijn sequence encoding. A De Bruijn sequence of order n over an alphabet of k color symbols is a cyclic sequence of length k^n with a so-called window property that each subsequence of length n appears exactly once [26].

Let $\mathcal{C} = \{1, 2, \dots, 8\}$ be the set of encoding color primitives, each number represent a different color. In particular, red(1), lime(3), cyan(5) and purple(7) are used for the horizontal stripes, while yellow(2), green(4), blue(6) and magenta(8) for vertical, e.g. as shown in Fig. 3, the vertical color stripes are (4, 8, 2) from left to right, the horizontal stripes are (1, 3, 7) from top to bottom. The selected colors’ hue values are evenly distributed in the HSV space for better color detection.

We employ De Bruijn encoding to both vertical and horizontal

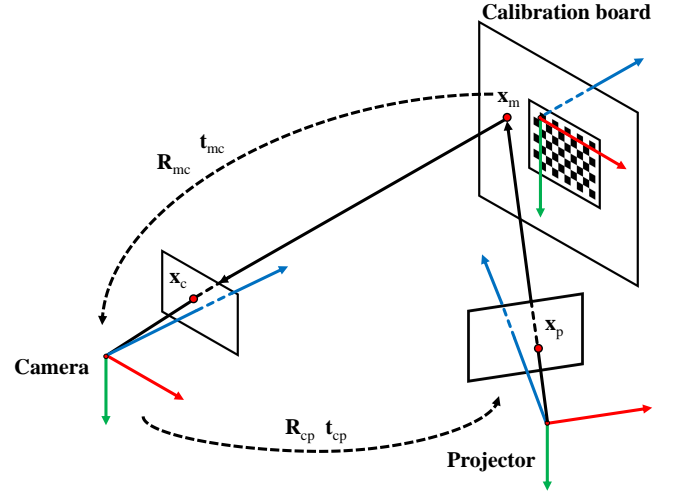


Figure 4: Coordinate system. The world origin is at the camera optical center. Red, green and blue axes represent X, Y and Z directions, respectively.

stripes, and construct a color grid with $m \times m$ intersections, where $m = k^n + 2$, in our case $k = 4, n = 3$. More importantly, a unique k -color horizontal sequence overlain atop a unique k -color vertical sequence only occurs once in the grid. As shown in inset of Fig. 3, this 3×3 subset color grid appears only once in the whole pattern. We represent the color-coded pattern using an undirected graph $\mathcal{G} = (\mathcal{V}, \mathcal{E})$, in which

- $\mathcal{V} = \{\mathbf{v}_1, \mathbf{v}_2, \dots, \mathbf{v}_{m \times m}\}$ is a set of graph nodes, which represent color stripes intersections, where

$$\mathbf{v}_i = \{\mathbf{x}_c(i), \mathbf{x}_p(i), \mathbf{x}_m(i)\}, \quad (1)$$

such that $\mathbf{x}_c(i) = [u_c(i), v_c(i)]^T$, $\mathbf{x}_p(i) = [u_p(i), v_p(i)]^T$, and $\mathbf{x}_m(i) = [x_m(i), y_m(i), z_m(i)]^T$ represent the coordinates of the i^{th} node in, respectively, the camera image space, the projector image space and the calibration board model space.

- $\mathcal{E} = \{\mathbf{e}_{00}, \mathbf{e}_{01}, \dots, \mathbf{e}_{ij}, \dots, \mathbf{e}_{m^2 \times m^2}\}$ is the set of all edges representing color stripe segments. We have $\mathbf{e}_{ij} = \{\mathcal{L}, \tau\}$, where \mathcal{L} is a list of pixels belonging to this edge and $\tau \in \mathcal{C} \cup \{0\}$ is the color label of the edge (if the link exists) or 0 (otherwise).

3.3 Finding Structured Light Correspondences

The correspondences between the camera captured image and the projected SL pattern is built by decoding the color codeword of the SL pattern (i.e. the De Bruijn pattern). It contains seven steps (Fig. 6) described below. More details are given in the supplementary material.

Step 1, the camera captures an image of the calibration board with color-encoded SL pattern on it. **Step 2**, the checkerboard area is cropped by removing the largest connected component of the binarized image. Then we threshold the image in channel V in the HSV space to get a binary mask. **Step 3**, we skeletonize the binary mask. **Step 4**, we model the skeleton image as an undirected graph \mathcal{G} with nodes \mathcal{V} and edges \mathcal{E} . The graph is traversed to find each node \mathbf{v}_i 's neighbors \mathbf{v}_j and edges \mathbf{e}_{ij} by breadth-first search (BFS). **Step 5**, we then mask SL stripes using the binary mask. After that the colors are enhanced using histogram equalization. **Step 6**, a k-means clustering algorithm is applied to cluster all pixel colors. We set number of clusters to 4 for both horizontal and vertical edges. The codeword of each node is formed by its six neighbor color stripes, both vertical and horizontal. **Step 7**, the correspondences of

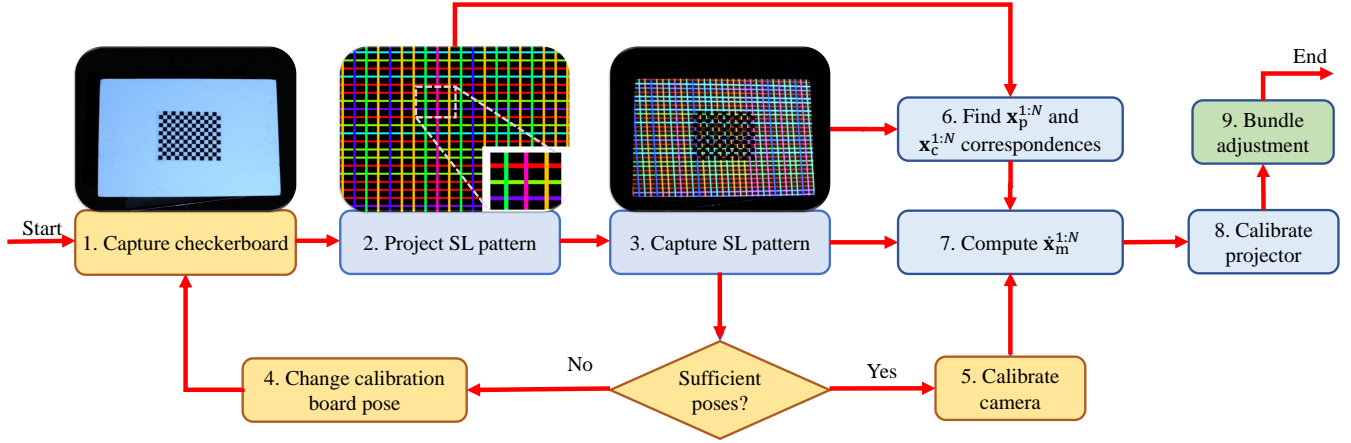


Figure 5: System flowchart. We divide the calibration algorithm into three procedures (Algorithm 1): **Yellow blocks**: camera initial calibration. **Blue blocks**: projector initial calibration and **Green block**: bundle adjustment. Best viewed in color.

Algorithm 1 The proposed calibration algorithm

```

1: Input: camera captured images  $\mathcal{J}^{1:N}$ 
2: Output: camera-projector pair parameters  $\hat{\Psi}$ 
3: // Stage 1. Initial Camera Calibration
4:  $\mathbf{K}_c, \mathbf{d}_c, \mathbf{R}_{mc}^{1:N}, \mathbf{t}_{mc}^{1:N} \leftarrow \text{ZhangCalib}(\mathcal{J}^{1:N})$ 
5: for  $j \leftarrow 1$  to  $N$  do
6:    $\mathbf{H}^j = \mathbf{K}_c * [\mathbf{r1}_{mc}^j, \mathbf{r2}_{mc}^j, \mathbf{t}_{mc}^j]$ 
7: // Stage 2. Initial Projector Calibration
8: for  $j \leftarrow 1$  to  $N$  do
9:    $\bar{\mathbf{x}}_c^j \leftarrow \text{undistort}(\mathbf{x}_c^j, \mathbf{d}_c)$ 
10:  for  $i \leftarrow 1$  to  $M^j$  do
11:     $\hat{\mathbf{x}}_m^j(i) = \text{inv}(\mathbf{H}^j) * \bar{\mathbf{x}}_c^j(i)$ 
12:   $\mathbf{K}_p, \mathbf{d}_p, \mathbf{R}_{mp}^{1:N}, \mathbf{t}_{mp}^{1:N} \leftarrow \text{ZhangCalib}(\hat{\mathbf{x}}_m^{1:N}, \bar{\mathbf{x}}_p^{1:N})$ 
13:   $\mathbf{R}_{cp} = \text{median}(\mathbf{R}_{mp}^{1:N} * (\mathbf{R}_{mc}^{1:N})^T)$ 
14:   $\mathbf{t}_{cp} = \text{median}(\mathbf{t}_{mp}^{1:N} - \mathbf{R}_{mp}^{1:N} * (\mathbf{R}_{mc}^{1:N})^T * \mathbf{t}_{mc}^{1:N})$ 
15: // Stage 3. Bundle Adjustment
16:  $\hat{\Psi} = [\mathbf{K}_c, \mathbf{d}_c, \mathbf{R}_{mc}^{1:N}, \mathbf{t}_{mc}^{1:N}, \mathbf{K}_p, \mathbf{d}_p, \mathbf{R}_{cp}, \mathbf{t}_{cp}, \hat{\mathbf{x}}_m^{1:N}]$ 
17:  $\hat{\Psi} \leftarrow \text{bundleAdjust}(\hat{\Psi})$ 
18: return  $\hat{\Psi}$ 

```

each node \mathbf{v}_i is found by matching the decoded codeword to a Look Up Table (LUT) of the De Bruijn sequence.

Once we have the camera and projector coordinates of all the nodes, we apply the homography \mathbf{H}^j to transform node points from the camera image plane to the calibration board model space, where \mathbf{H}^j is the transformation for the j -th pose estimated by initial calibration (Sect. 3.4).

3.4 Initial Calibration

The camera and projector view spaces and calibration board model space follow a right hand coordinate system as shown in Fig. 4. The world origin is at the camera optical center.

Camera and Projector Model We employ the pin-hole model for both camera and projector calibration, with intrinsic matrices

denoted by \mathbf{K}_c and \mathbf{K}_p , respectively:

$$\mathbf{K}_c = \begin{bmatrix} f_x & 0 & c_x \\ 0 & f_y & c_y \\ 0 & 0 & 1 \end{bmatrix}, \quad \mathbf{K}_p = \begin{bmatrix} f'_x & 0 & c'_x \\ 0 & f'_y & c'_y \\ 0 & 0 & 1 \end{bmatrix}, \quad (4)$$

where f_x, f'_x and f_y, f'_y represent camera and projector focal lengths in x and y directions. (c_x, c_y) and (c'_x, c'_y) represent camera and projector image principle coordinates. The camera and projector distortion coefficients are given by:

$$\mathbf{d}_c = [k_1, k_2, p_1, p_2], \quad \mathbf{d}_p = [k'_1, k'_2, p'_1, p'_2], \quad (5)$$

where k_1, k'_1 and k_2, k'_2 are radial distortion factors; p_1, p'_1 and p_2, p'_2 are tangential distortion factors.

In addition, we model extrinsics parameters, i.e., relative rotation and translation of the camera with respect to the projector as:

$$\mathbf{r}_{cp} = (r_x, r_y, r_z)^T, \quad \mathbf{t}_{cp} = (t_x, t_y, t_z)^T. \quad (6)$$

Note that $\mathbf{r}_{cp} \in \mathfrak{so}(3)$ is a rotation vector, i.e., the associated Lie algebra of rotation matrix $\mathbf{R}_{cp} \in \text{SO}(3)$.

Camera Calibration We first calibrate the camera using Zhang's method [34], with all the checkerboard corner correspondences from camera images $\{\mathcal{J}^1, \mathcal{J}^2, \dots, \mathcal{J}^N\}$ to the calibration board model space. We obtain initial guess of camera intrinsics \mathbf{K}_c and \mathbf{d}_c , as well as relative rotation \mathbf{R}_{mc}^j and translation \mathbf{t}_{mc}^j between the j^{th} calibration board pose and the camera view space. A homography \mathbf{H}^j between the calibration board and the camera image plane can then be calculated by Equation 2, where $\mathbf{r1}_{mc}^j$ and $\mathbf{r2}_{mc}^j$ are the 1^{st} and 2^{nd} columns of \mathbf{R}_{mc}^j of the j^{th} pose.

Projector Calibration As shown in Fig. 5, we transform the SL pattern nodes from camera image space to calibration board model space by Equation 3 in Algorithm 1, where $\bar{\mathbf{x}}_c^j(i)$ is the undistorted homogeneous coordinates of node \mathbf{v}_i in the camera image space, imaged at the j^{th} pose. To be clear, we do not use checkerboard corners for projector calibration, instead we employ the SL nodes since they provide more robust and accurate initial guess.

Once we obtained the node point pairs $(\hat{\mathbf{x}}_m, \bar{\mathbf{x}}_p)$, Zhang's method is applied to calibrate the projector parameters, as shown in line 12 of Algorithm 1. The relative translation and rotation between camera and projector are computed as shown in lines 13-14 of Algorithm 1.

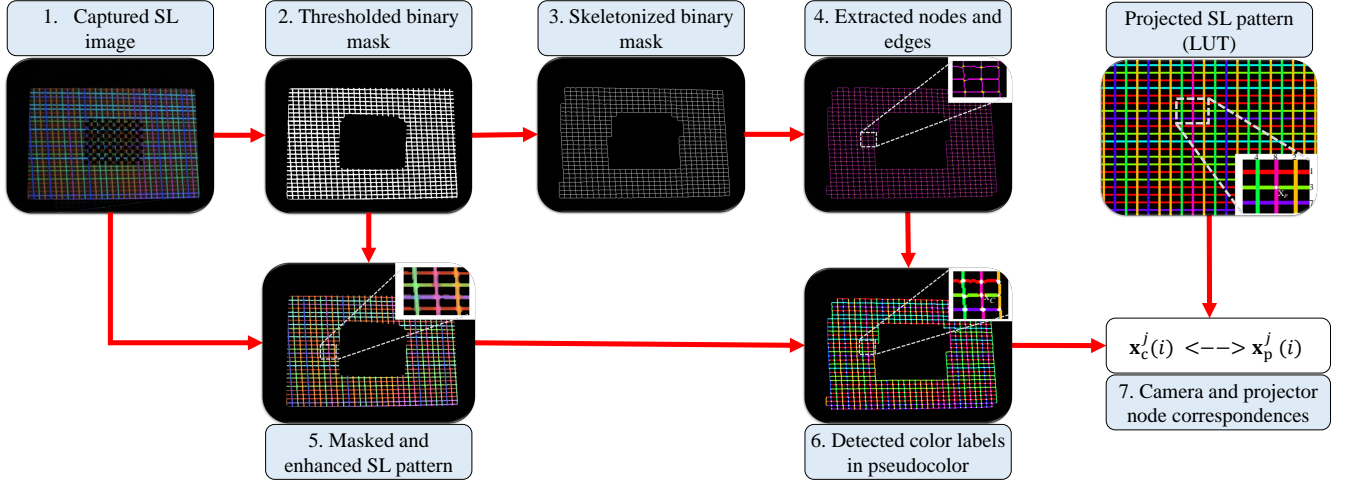


Figure 6: Finding SL correspondences (expansion of step 6 in Fig. 5). The goal is to find the coordinates of a node \mathbf{v}_i in both camera and projector image spaces. Best viewed in color.

3.5 Bundle Adjustment

As illustrated in Fig. 2, the imperfect planarity of the calibration board can bring errors to the initial calibration. Attacking this problem, given the initial camera and projector calibration, we propose a bundle adjustment (BA) algorithm (Stage 3 of Algorithm 1) on the initial intrinsics and extrinsics, as well as node point coordinates $\mathbf{x}_m^{1:N}$ subject to reprojection errors. The result is shown as the blue plane (Fig. 2), which is much closer to the cyan ground truth than previous solutions.

Specifically, we set the world origin at camera optical center and let camera and projector parameters be:

$$\Psi_c = (\mathbf{K}_c, \mathbf{d}_c, \mathbf{r}_{mc}^{1:N}, \mathbf{t}_{mc}^{1:N}) \quad (7)$$

$$\Psi_p = (\mathbf{K}_p, \mathbf{d}_p, \mathbf{r}_{cp}, \mathbf{t}_{cp}), \quad (8)$$

where $\mathbf{r}_{mc}^{1:N}$ and $\mathbf{t}_{mc}^{1:N}$ are relative rotation and translation vectors of the calibration board with respect to the camera; $\mathbf{r}_{cp}, \mathbf{t}_{cp}$ are relative rotation and translation of the camera with respect to the projector.

Now, the camera-projector calibration problem can be formulated as minimizing the following BA cost:

$$\{\hat{\Psi}_c, \hat{\Psi}_p, \hat{\mathbf{x}}_m^{1:N}\} = \arg \min_{\Psi_c, \Psi_p, \mathbf{x}_m^{1:N}} (\text{cost}(\Psi_c, \Psi_p, \mathbf{x}_m^{1:N})), \quad (9)$$

More specifically, suppose the j^{th} calibration board pose has M^j nodes imaged on the calibration board, and denote $n_p = \sum_{j=1}^N M^j$. The objective function is formulated as:

$$\text{cost} = \sum_{j=1}^N \sum_{i=1}^{M^j} (\delta_c^j(i) + \delta_p^j(i) + \lambda \delta_m^j(i)). \quad (10)$$

The first two terms represent reprojection errors of the node \mathbf{v}_i in camera and projector image space:

$$\delta_c^j(i) = \|\mathbf{x}_c^j(i) - f(\Psi_c; \mathbf{x}_m^j(i))\|^2 \quad (11)$$

$$\delta_p^j(i) = \|\mathbf{x}_p^j(i) - f(\Psi_p, \mathbf{r}_{mc}^{1:N}, \mathbf{t}_{mc}^{1:N}; \mathbf{x}_m^j(i))\|^2, \quad (12)$$

where $f: \mathbb{R}^3 \mapsto \mathbb{R}^2$ projects a node coordinate $\mathbf{x}_m^j(i)$ from the calibration board model space to the camera/projector image space using camera/projector parameters.

In addition, we add a scale constraint that bounds the scale of model point coordinates during bundle adjustment:

$$\delta_m^j(i) = \|\hat{\mathbf{x}}_m^j(i) - \dot{\mathbf{x}}_m^j(i)\|^2 \quad (13)$$

This term is necessary since the model point coordinates are coupled with extrinsic parameters \mathbf{r}_{cp} and \mathbf{t}_{cp} . The original model point coordinates $\dot{\mathbf{x}}_m^j(i)$ are computed by Equation 3. We introduce a weight λ to control the weight of the scale constraint, and empirically set $\lambda = \exp(-\delta_m^j(i))$.

We apply the trust-region-reflective algorithm to solve for Equation 9. Since we introduce n_p node model coordinates \mathbf{x}_m to bundle adjustment, leading $3 \times n_p$ extra parameters to optimize, a sparse Jacobian matrix pattern is designed to speed up numerical finite derivative computation.

4 EXPERIMENTS AND RESULTS

Our camera-projector pair consists of an Intel RealSense F200 RGB-D camera with image resolution of 640×480 , and an Optima 66HD DLP projector set to the resolution of 800×600 , as shown in Fig. 1. Note we only use RGB camera for calibration and reconstruction, the depth camera is employed only for generating ground truth. The camera is located at about two meters away from the calibration board, and about one meter away from the projector.

4.1 Evaluated Baselines

We compare our method with three other methods: a generalized global homography method, a multi-shot local homography method [17], and a degenerated baseline of the proposed method.

To compare with other camera-projector calibration methods (e.g. [31]), it is inevitable to have to apply their calibration patterns (e.g. the ARTags pattern) and configurations. It is hard to make a fair comparison this way. Instead, we generalize a method named **Global homography** to represent global homography-based methods in our experimental configuration. Specifically, since most existing global homography based methods use OpenCV's implementation of [34], **Global homography** starts by calibrating the camera using OpenCV's `calibrateCamera` function, and then estimates a global homography to transform undistorted printed pattern points from the camera image to the projector image, followed by calibrating the projector using the same way for camera. Finally we find relative rotation and translation between camera and projector using `stereoCalibrate` in OpenCV.

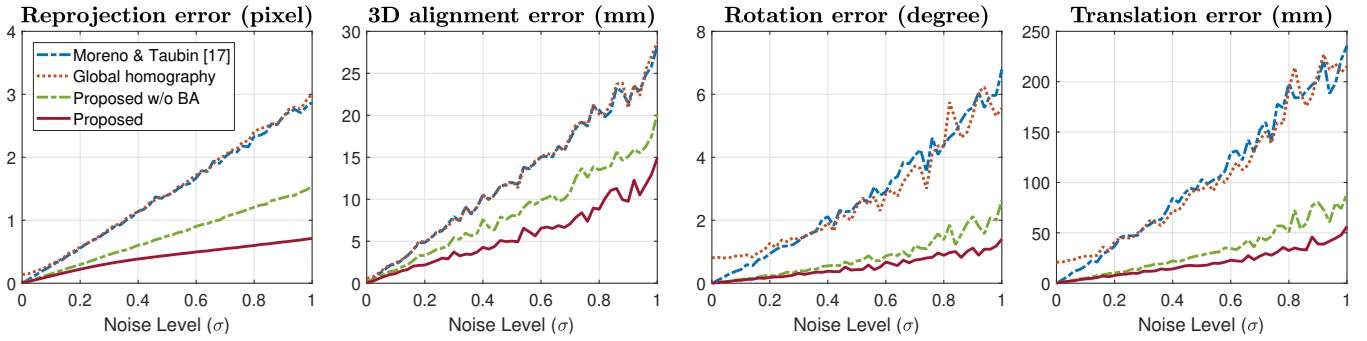


Figure 7: Reprojection, 3D alignment, rotation and translation errors when noise level $\sigma = 0 \rightarrow 1$.

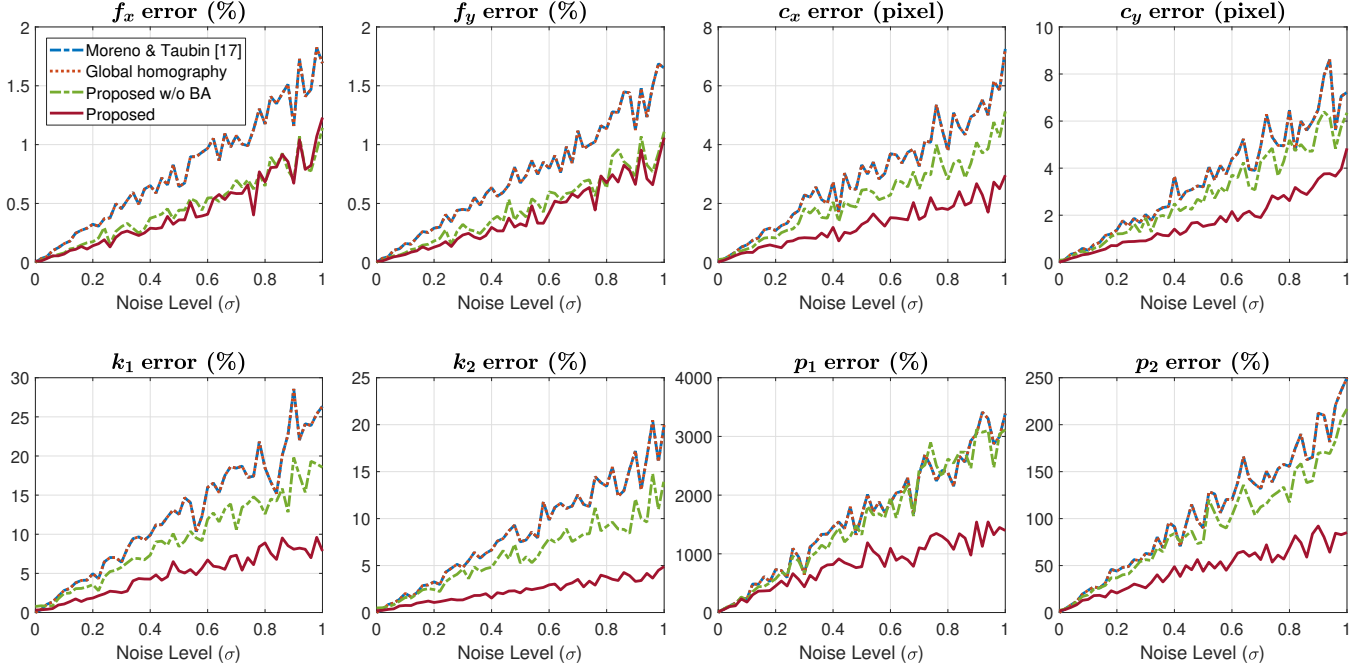


Figure 8: Errors in **camera intrinsics** for different noise levels $\sigma = 0 \rightarrow 1$. f_x and f_y are camera focal lengths in two directions, (c_x, c_y) is the camera image principle point, and k_1, k_2 and p_1, p_2 are radial and tangential distortion factors, respectively.

For local homography based method, we employ the popular system by **Moreno & Taubin** [17] with default parameters.

In addition, we generate a degraded version of the proposed algorithm by excluding the BA stage, named as **Proposed w/o BA**. In particular, this baseline only includes $\mathbf{r}_{mc}^{1:N}$ and $\mathbf{t}_{mc}^{1:N}$ in the nonlinear optimization. Unlike **Global homography** that uses points from a checkerboard, the degraded method applies points from an SL pattern. This strategy boosts not only the number of feature points but also their spatial distribution, and hence is more robust and accurate than **Global homography**.

The three methods are tested together with the proposed one using both synthetic and real data. Root mean square (RMS) reprojection errors, 3D alignment errors, intrinsics and extrinsics errors are used as criteria. The synthetic data results (Fig. 7-Fig. 9) and real data results (Fig. 10) show clearly the benefits of the proposed method.

To compare the proposed method with baseline methods statistically, we first use synthetic data as benchmarks, where the camera and projector intrinsics and extrinsics, checkerboard corners and calibration board geometry are known. In particular, synthetic data provides absolute ground truth and accurate error measurement.

We start by generating the data by projecting the projector SL

patterns to the world space. Each pair of node coordinate in projector image space \mathbf{x}_p and projector optical center forms a ray that intersects with a set of predefined calibration boards, those intersections represent node's coordinates in the calibration board model space \mathbf{x}_m . Next we project \mathbf{x}_m to the camera image space using pre-defined camera intrinsics and extrinsics, obtaining node's coordinates in camera image space \mathbf{x}_c . Finally, we follow the steps in Algorithm 1 to calibrate our camera-projector pair.

We add Gaussian white noise with zero mean and standard deviation of σ to both camera and projector images. It is worth noting that, to simulate imperfect planarity, we also add Gaussian white noise to checkerboard and SL nodes in calibration board model space, whereas the noise units are in millimeters (mm). We generate the statistical benchmarks by inspecting the RMS reprojection errors, 3D alignment errors, intrinsics errors and extrinsics errors at each noise level $\sigma = 0 \rightarrow 1$. The 3D alignment errors are discrepancies between a synthetic 3D geometry and reconstructed 3D geometry.

The experiments are performed 100 times for each noise level σ and we plot the median of the errors as shown in Fig. 7 to Fig. 9. The proposed method clearly outperforms the three methods in comparison. Moreover, **Global homography** method's reprojection

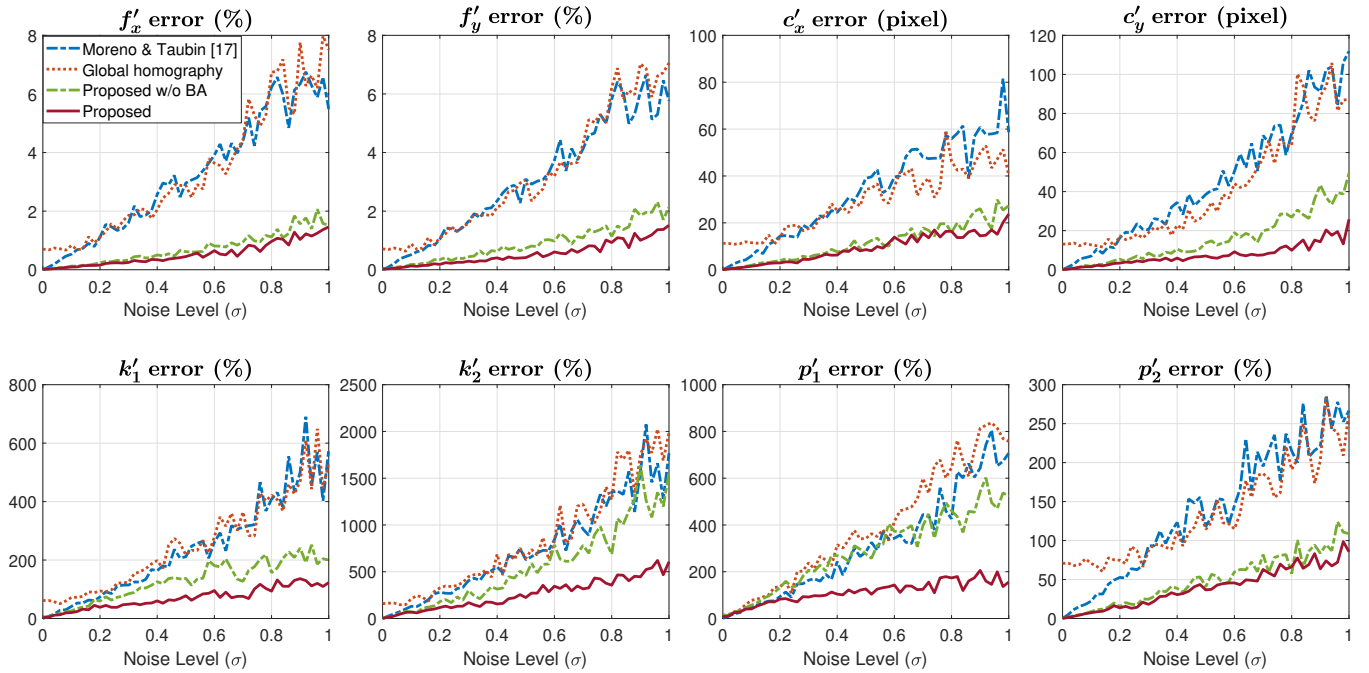


Figure 9: Errors in **projector intrinsics** for different noise levels $\sigma = 0 \rightarrow 1$. f'_x and f'_y are projector focal lengths in two directions. (c'_x, c'_y) is the projector image principle point, and k'_1, k'_2 and p'_1, p'_2 are radial and tangential distortion factors, respectively.

Table 2: RMS reprojection errors of camera, projector and stereo calibrations (pixel).

Method	Camera	Projector	Stereo
Moreno & Taubin [17]	0.1212	1.7053	1.7096
Global homography	0.1212	4.4601	4.4617
Proposed w/o BA	0.1579	0.4982	0.5226
Proposed	0.1676	0.2574	0.3072

error, rotation error, translation error and some projector intrinsics errors are nonzero even when the noise level $\sigma = 0$ due to its inability to model projector lens distortions. In Fig. 8, **Global homography**'s and **Moreno & Taubin**'s curves overlap because they apply the same camera calibration method to the same set of checkerboard points.

4.2 Real Data

In this section, we evaluate our calibration using an imperfect planar white board with a printed checkerboard pattern glued to it. As shown in Table 2, the proposed method is able to refine imperfect planar model points and inaccurate camera parameters using bundle adjustment, thus leading to lower projector and stereo RMS reprojection errors than its competitors.

It is worth noting that the projector RMS reprojection errors of the first two methods are high for two reasons: (1) they use Zhang's method to calibrate the camera-projector pair and thus suffer from imperfectness in the planarity of the calibration board. (2) The errors of extrinsics, i.e., \mathbf{R}_{cp} and \mathbf{t}_{cp} , propagate to the projector (see Equation 8 and Equation 12), leading to enlarged high RMS reprojection errors.

One may notice that our camera reprojection error is a bit higher than the other two methods. This is because projected SL nodes are used for camera-projector calibration, while the reprojection errors are based on nodes rather than checkerboard points. Namely, reprojection errors solely are not sufficient to represent calibration

accuracy if different set of points are employed. Thus, we evaluate reconstruction errors (Table 3) by comparing the reconstructed point cloud with the ground truth. We first employ the calibration data from the methods in Table 2 to reconstruct a point cloud using SL. Then the reconstruction errors are calculated as the RMS discrepancies between the SL reconstructed point cloud and the RGB-D camera captured point cloud.

Our method outperforms both global and local homography based methods on projector and stereo RMS reprojection errors and reconstruction errors. Our single-shot method also overcomes the drawbacks of requiring many shots per pose, whereas **Moreno & Taubin** [17] needs 20 shots per pose, and one local homography per checkerboard corner. Additionally, Audet *et al.* [3] needs at least two shots per pose for prewarp and additional time for incremental adjustment.

We employ the calibrated camera-projector pair to reconstruct three objects using SL. As shown in Fig. 10, a paper box, a plaster bust and a folded paper board are reconstructed using the calibration data of the four evaluated methods. The statistics of reconstruction errors are given in Table 3, the **proposed w/o BA** method outperforms **Global homography** and **Moreno & Taubin** [17], since it applies SL nodes to calibration. The **proposed** method outperforms the degraded version, because BA is able to compensate for imperfect nonplanarity.

5 CONCLUSIONS

In this paper we present a flexible single-shot camera-projector calibration method. Compared with existing calibration systems, our method has two advantages: (1) Both synthetic and real data demonstrate that our method can refine imperfectly calibrated camera/projector parameters and imperfect planar calibration board points, thus leading to higher calibration accuracy and robustness against noises in planarity. (2) Requiring only a single shot of SL pattern per pose, our system enables fast and efficient calibration, especially in applications that need frequent re-calibration. Furthermore, the one-shot calibration provides a flexible and accurate

Table 3: Reconstruction errors (mm) of real objects.

Method	Paper box			Plaster bust			Folded paper board		
	Mean	Median	Std.	Mean	Median	Std.	Mean	Median	Std.
Moreno & Taubin [17]	10.05	8.31	7.00	13.73	11.53	9.51	29.47	27.84	19.06
Global homography	18.52	19.30	5.17	11.45	11.46	4.56	25.33	24.76	11.60
Proposed w/o BA	9.56	9.01	4.72	3.98	3.34	3.30	11.06	10.49	6.93
Proposed	5.93	5.31	3.95	3.48	2.38	3.47	8.35	6.87	5.82

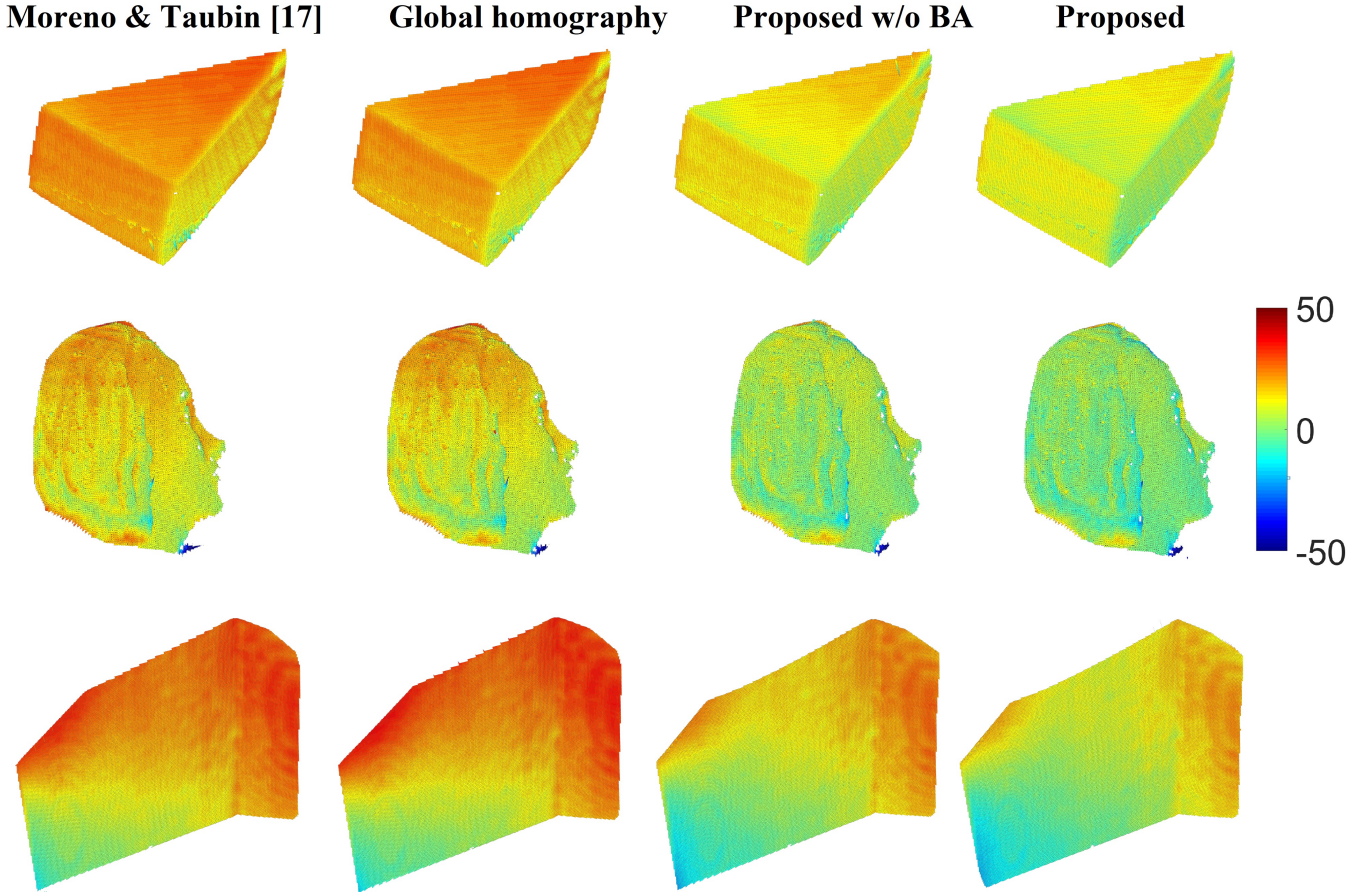


Figure 10: Reconstructed paper box (1st row), plaster bust (2nd row) and folded paper board (3rd row) using a camera-projector pair calibrated by the four calibration methods. Reconstruction errors (mm) are shown in pseudocolor.

results even when the board is handheld.

REFERENCES

- [1] A. Albarelli, E. Rodolà, and A. Torsello. Robust Camera Calibration using Inaccurate Targets. In *BMVC*, pp. 16.1–16.10, 2010. doi: 10.5244/C.24.16
- [2] H. Anwar, I. Din, and K. Park. Projector calibration for 3D scanning using virtual target images. *International Journal of Precision Engineering and Manufacturing*, 13:125–131, 2012. doi: 10.1007/s12541-012-0017-3
- [3] S. Audet and M. Okutomi. A user-friendly method to geometrically calibrate projector-camera systems. In *CVPRW*, pp. 47–54, 2009. doi: 10.1109/CVPR.2009.5204319
- [4] A. Ben-Hamadou, C. Soussen, C. Daul, W. Blondel, and D. Wolf. Flexible calibration of structured-light systems projecting point patterns. *Computer Vision and Image Understanding*, 117:1468–1481, 2013. doi: 10.1016/j.cviu.2013.06.002
- [5] N. Bird and N. Papanikolopoulos. Optimal Image-Based Euclidean Calibration of Structured Light Systems in General Scenes. *IEEE TASE*, 8:815–823, 2011. doi: 10.1109/TASE.2011.2144583
- [6] C.-Y. Chen and H.-J. Chien. An Incremental Target-Adapted Strategy for Active Geometric Calibration of Projector-Camera Systems. *Sensors*, 13:2664–2681, 2013. doi: 10.3390/s130202664
- [7] D. S. Dhillon and V. M. Govindu. Geometric and radiometric estimation in a structured-light 3D scanner. *Machine Vision and Applications*, 26:339–352, 2015. doi: 10.1007/s00138-015-0667-0
- [8] J. Drareni, S. Roy, and P. Sturm. Geometric video projector auto-calibration. In *CVPRW*, pp. 39–46, 2009. doi: 10.1109/CVPR.2009.5204317
- [9] M. Fiala. Automatic Projector Calibration Using Self-Identifying Patterns. In *CVPRW*, vol. 3, pp. 113–113, 2005. doi: 10.1109/CVPR.2005.416
- [10] J. Geng. Structured-light 3D surface imaging: a tutorial. *Advances in Optics and Photonics*, 3:128, 2011. doi: 10.1364/AOP.3.000128
- [11] B. Huang and Y. Tang. Fast 3D reconstruction using one-shot spatial structured light. In *IEEE International Conference on Systems, Man, and Cybernetics (SMC)*, pp. 531–536, 2014. doi: 10.1109/SMC.2014.6973962

- [12] L. Huang, Q. Zhang, and A. Asundi. Flexible camera calibration using not-measured imperfect target. *Applied Optics*, 52:6278, 2013. doi: 10.1364/AO.52.006278
- [13] Z. Huang, J. Xi, Y. Yu, and Q. Guo. Accurate projector calibration based on a new point-to-point mapping relationship between the camera and projector images. *Applied Optics*, 54:347, 2015. doi: 10.1364/AO.54.000347
- [14] M. Kimura, M. Mochimaru, and T. Kanade. Projector Calibration using Arbitrary Planes and Calibrated Camera. In *CVPR*, pp. 1–2, 2007. doi: 10.1109/CVPR.2007.383477
- [15] F. Li, H. Sekkati, J. Deglint, C. Scharfenberger, M. Lamm, D. Clausi, J. Zelek, and A. Wong. Simultaneous Projector-Camera Self-Calibration for Three-Dimensional Reconstruction and Projection Mapping. *IEEE TCI*, 3:74–83, 2017. doi: 10.1109/TCI.2017.2652844
- [16] T. T. Li, H. Y. Zhang, and J. Geng. Geometric calibration of a camera-projector 3D imaging system. *International Conference Image and Vision Computing New Zealand*, 2010. doi: 10.1109/IVCNZ.2010.6148798
- [17] D. Moreno and G. Taubin. Simple, Accurate, and Robust Projector-Camera Calibration. In *2012 Second International Conference on 3D Imaging, Modeling, Processing, Visualization & Transmission*, pp. 464–471, 2012. doi: 10.1109/3DIMPVT.2012.77
- [18] A. R. Orghidan, C. M. Gordan, D. A. Vlaicu, and B. J. Salvi. Projector-camera calibration for 3D reconstruction using vanishing points. In *IC3D*, pp. 1–6, 2012. doi: 10.1109/IC3D.2012.6615143
- [19] J.-N. Ouellet, F. Rochette, and P. Hbert. Geometric calibration of a structured light system using control points circular. In *3DPVT*, pp. 183–190, 2008.
- [20] T. Petkovic, T. Pribanic, and M. Donlic. Single-Shot Dense 3D Reconstruction Using Self-Equalizing De Bruijn Sequence. *IEEE TIP*, 25:5131–5144, 2016. doi: 10.1109/TIP.2016.2603231
- [21] C. Resch, H. Naik, P. Keitler, S. Benkhardt, and G. Klinker. On-Site Semi-Automatic Calibration and Registration of a Projector-Camera System Using Arbitrary Objects with Known Geometry. *IEEE TVCG*, 21:1211–1220, 2015. doi: 10.1109/TVCG.2015.2459898
- [22] J. Salvi, J. Batlle, and E. Mouaddib. A robust-coded pattern projection for dynamic 3D scene measurement. *Pattern Recognition Letters*, 19:1055–1065, 1998. doi: 10.1016/S0167-8655(98)00085-3
- [23] M. Shahpaski, L. Ricardo Sapaico, G. Chevassus, and S. Susstrunk. Simultaneous geometric and radiometric calibration of a projector-camera pair. In *CVPR*, 2017.
- [24] K. H. Strobl and G. Hirzinger. More accurate pinhole camera calibration with imperfect planar target. In *ICCVW*, pp. 1068–1075, 2011. doi: 10.1109/ICCVW.2011.6130369
- [25] W. Sun and J. R. Cooperstock. An empirical evaluation of factors influencing camera calibration accuracy using three publicly available techniques. *Machine Vision and Applications*, 17:51–67, 2006. doi: 10.1007/s00138-006-0014-6
- [26] T. van Aardenne-Ehrenfest and N. G. de Bruijn. Circuits and trees in oriented linear graphs. In *Classic papers in combinatorics*, pp. 149–163. Springer, 2009.
- [27] S. Willi and A. Grundhfer. Robust geometric self-calibration of generic multi-projector camera systems. In *2017 IEEE International Symposium on Mixed and Augmented Reality (ISMAR)*, pp. 42–51, Oct 2017. doi: 10.1109/ISMAR.2017.21
- [28] S. Yamazaki, M. Mochimaru, and T. Kanade. Simultaneous self-calibration of a projector and a camera using structured light. In *CVPRW*, pp. 60–67, 2011. doi: 10.1109/CVPRW.2011.5981781
- [29] L. Yang, J. M. Normand, and G. Moreau. Practical and precise projector-camera calibration. In *2016 IEEE International Symposium on Mixed and Augmented Reality (ISMAR)*, pp. 63–70, Sept 2016. doi: 10.1109/ISMAR.2016.22
- [30] B. Zhang, Y. Li, and Y. Wu. Self-recalibration of a structured light system via plane-based homography. *Pattern Recognition*, 40:1368–1377, 2007. doi: 10.1016/j.patcog.2006.04.001
- [31] L. Zhang, B. Curless, and S. M. Seitz. Rapid shape acquisition using color structured light and multi-pass dynamic programming. In *3DPVT*, pp. 24–37, 2002. doi: 10.1109/TDPVT.2002.1024035
- [32] S. Zhang and P. P. S. Huang. Novel method for structured light system calibration. *Optical Engineering*, 45:083601, 2006. doi: 10.1117/1.2336196
- [33] X. Zhang, Z. Zhang, and W. Cheng. Iterative projector calibration using multi-frequency phase-shifting method. In *2015 IEEE 7th International Conference on Cybernetics and Intelligent Systems (CIS) and IEEE Conference on Robotics, Automation and Mechatronics (RAM)*, pp. 1–6, 2015. doi: 10.1109/ICCIS.2015.7274538
- [34] Z. Zhang. A flexible new technique for camera calibration. *IEEE TPAMI*, 22:1330–1334, 2000. doi: 10.1109/34.888718